

## Viscosity-dependent swimming patterns assist *Aliivibrio fischeri* for symbiont partner finding

Xiang-Yu Zhuang , Chao-Kai Tseng, and Chien-Jung Lo \*

Department of Physics and Center for Complex Systems, National Central University, Zhong-Li, Taoyuan 32001, Taiwan  
and Institute of Physics, Academia Sinica, Taipei 11529, Taiwan

 (Received 31 January 2024; accepted 2 July 2024; published 26 August 2024)

Bacteria employ diverse swimming patterns for chemotaxis, influenced by factors including flagellar arrangements, motor rotation, flagellar filament configurations, and polymorphism. Understanding the chemotactic strategy of *Aliivibrio fischeri* in locating a squid partner is paramount for comprehending this highly species-specific symbiosis. In this study, we applied three-dimensional swimming tracking and real-time visualization of lophotrichous flagellar configurations. These techniques unveiled viscosity-dependent transitions in swimming patterns, shifting from push-pull to push-wrap modes. Notably, our research also revealed coupled flagellar switching and polymorphic transformations during the wrap mode, significantly extending *A. fischeri*'s backward swimming duration and, consequently, its overall runtime. This strategic adaptation allows *A. fischeri* to broaden its effective search range, particularly within high-viscosity environments like the squid light organ. In response to attractants, the coupling rate is reduced to facilitate efficient short-range searching. These innovative chemotactic strategies ensure precise navigation for *A. fischeri* in locating and colonizing its symbiotic partner, the squid *Euprymna scolopes*.

DOI: [10.1103/PhysRevResearch.6.033214](https://doi.org/10.1103/PhysRevResearch.6.033214)

### I. INTRODUCTION

Flagellar-assisted bacterial swimming serves as one of the most widespread mechanisms for single-cell locomotion [1–3], facilitating crucial activities such as nutrient search, infection, colony expansion, biofilm formation, and the discovery of symbiotic partners. The complete chemotaxis system involves a sophisticated interplay between chemoreceptors, which act as sensory tools, the signal transduction pathway, and the intricate flagellar motor systems. Bacterial flagella are far from being mere propulsion devices; they exhibit dynamic and complex behavior influenced by various factors, including flagellar arrangements, motor rotation direction (counterclockwise/clockwise/stop), flagellar filament configuration (tailed/wrapped/spread), and filament polymorphism [4]. Leveraging this complexity, bacteria navigate through a sequence of straight runs interspersed with turning events, creating a bacterial swimming pattern that can be likened to the concept of bacterial diffusion [4].

The underlying chemotactic behavior is a dynamic process in which cells modulate between random walk and biased random walk states in response to the temporal cues they collect from their surrounding environment. This modulation is achieved by orchestrating different motility states through flagellar motor rotation. For instance, the classic example of *Escherichia coli* relies on motor switching to perform

run-tumble modulation, which is particularly effective when paired with peritrichous flagellar arrangement [5]. In contrast, *Vibrio alginolyticus* utilizes a run-reverse-flick pattern to enhance its searching efficiency [6]. Recent discoveries involving the flagellar wrap mode have further expanded our understanding of bacterial motility, revealing its role in tasks such as obstacle evasion [7], surface gliding [8], and chemotaxis enhancement [9,10]. These findings indicate the crucial significance of comprehending bacterial three-dimensional (3D) swimming patterns and the complete spectrum of swimming states [11,12].

Unlike the deterministic klinotaxis of sperm cells [13], bacterial chemotaxis is traditionally considered to be stochastic. However, in many biological examples, the bacterial cells demonstrate precise navigation. For instance, lophotrichous bacterium *Aliivibrio fischeri* stands as a prime example, capable of effectively locating symbiotic partners through minute 10  $\mu\text{m}$  pores that lead to the light organ crypt [14–17]. The few millimeter journey of planktonic *A. fischeri* cells starts from the seawater and migrates through the mucus region of ciliated appendages with attractants to the entrance of the light organ crypt of newly hatched squid. These adaptable microorganisms regularly face changing environments characterized by variations in temperature, chemicals, and viscosity, such as transitions from free swimming in open water to confined environments like infection sites or mucous-rich surroundings.

In this article, we present a detailed examination of the 3D motility of *A. fischeri*, unveiling its viscosity-dependent swimming patterns. In aquatic conditions, *A. fischeri* utilizes a push-pull swimming strategy. However, when navigating through higher viscosity environments, the motor switching induced simultaneous flagellar polymorphic transformations come into play, effectively trapping the bacterium in the wrap mode and significantly extending its runtime. This

\*Contact author: [cjlo@phy.ncu.edu.tw](mailto:cjlo@phy.ncu.edu.tw)

Published by the American Physical Society under the terms of the Creative Commons Attribution 4.0 International license. Further distribution of this work must maintain attribution to the author(s) and the published article's title, journal citation, and DOI.

adaptability allows *A. fischeri* to increase its effective search range and enhance its overall diffusivity in high-viscosity settings. In light of these discoveries, we have developed an active particle model for simulation, revealing a remarkably high degree of chemotactic efficiency in locating symbiotic partners. These findings not only have implications for technical advancements but also contribute to a deeper understanding of the dynamic operation of flagella, shedding light on an essential aspect of bacterial locomotion.

## II. METHODS

### A. Cell culturing

The *A. fischeri* strain ATCC7744 was cultured from  $-80^{\circ}\text{C}$  frozen stock in LBS medium, comprising 1% Bacto-Tryptone, 0.5% Yeast-Extract, 342 mM NaCl, 5% 1 M Tris-HCl (pH 7.5), and incubated at  $25^{\circ}\text{C}$  for 14–16 h [19]. Subsequently, the overnight culture was diluted at a 1:100 ratio in a  $\text{Mg}^{2+}$ -regulated medium, consisting of 1% Bacto-Tryptone, 300 mM NaCl, 2 mM  $\text{MgSO}_4$  and further incubated at  $25^{\circ}\text{C}$  for 4.5 h. Although  $\text{Mg}^{2+}$  ions are known to play a crucial role in flagellar growth in *A. fischeri* [20,21], however, in the  $\text{Mg}^{2+}$ -regulated medium, ranging from 2 mM to 50 mM, there is no interference with the bacterial growth process or the characteristic size of the bacteria.

### B. Sample preparation

The subcultured cells were harvested by centrifugation at 5500 rpm for 2 min. Following this, they were gently washed in TMN300 buffer, composed of 300 mM NaCl, 5 mM  $\text{MgCl}_2$ , 5 mM glucose, and 50 mM Tris-HCl (pH 7.5). Microscope tunnel slides were assembled by affixing three-layer double-sided adhesive tapes between standard microscope slides ( $75 \times 26$  mm, top side) and coverslips ( $24 \times 40$  mm, bottom side). The coverslips were treated by sonicating them in a saturated KOH solution with 50% ethanol for 10 min, followed by thorough rinsing with deionized water. They were then dried in a clean hood.

### C. Microscopy

We utilized an inverted microscope (Nikon, Ti2-E) equipped with an LED light source (Omicron, LedHub), a high-speed camera (Andor, Zyla 4.2 plus), and Nikon NIElements software (version 4.51) for our experimental setup. In our 3D tracking experiments, we employed a Nikon S Fluor Plan  $40\times$  Ph2 ADM objective, while for fluorescence experiments a Nikon Apo TIRF  $100\times$  Oil objective was used. For fluorescence imaging, we constructed a fluorescence cube consisting of a 470/40 nm bandpass filter for excitation, a dichroic mirror with a center wavelength of 491 nm, and a 510 nm long-pass emission filter.

### D. 3D tracking microscopy

To induce spherical distortion, the correction collar of a Nikon  $40\times$  phase-contrast objective was set to 1.2 mm to achieve the optimal signal-to-noise ratio [as shown in the Supplemental Material (SM) [22], Fig. S1A]. We adopted the foundational algorithm established in a prior publication

by Taute *et al.* in 2015 [18]. However, we made a notable modification by replacing the image reference libraries with images of *A. fischeri* cells. This change was necessary to account for the phase difference between beads and real cells, which would influence the depth response curve (see SM [22], Fig. S1B). To obtain the real cell image libraries, *A. fischeri* cells were immobilized in a TMK300 buffer containing 300 mM KCl, 5 mM  $\text{MgCl}_2$ , 5 mM glucose, and 50 mM Tris-HCl (pH 7.5). The cells were immobilized on a surface coated with 0.01% poly-L-lysine. Subsequently, a motorized stage was used to scan the depth phase pattern at 50 nm intervals. The reconstructed image reference libraries were generated using a Z-scan setup with a step size of 50 nm, a range of 120  $\mu\text{m}$ , and included data from 114 cells.

### E. Strobe fluorescence microscopy

The cell membrane and flagella of *A. fischeri* were fluorescently labeled with 16  $\mu\text{M}$  FM 1-43 in a suitable buffer, as described in Zhuang [23]. Fluorescence images were captured using a high-speed camera operating at a 33/100 frames per second (fps) acquisition rate, with strobe excitation set to a 0.5%/2% duty cycle (150/200  $\mu\text{s}$  pulse width). Synchronization of image capture and excitation was achieved using a National Instruments data acquisition device (NI-DAQ, USB-6221) to control both the camera (Andor, Zyla 4.2 PLUS) and the excitation light source (Omicron, LedHUB) through pulse-width modulation (PWM) signals.

## III. RESULTS

### A. 3D tracking and swimming modes

*A. fischeri* is a fast-swimming marine bacterium with multiple polar flagella. To capture full swimming 3D trajectories, we used high-throughput 3D bacterial tracking [18] to observe *A. fischeri* swimming patterns. The phase-contrast 3D tracking is based on an induced asymmetric point spread function (PSF) for  $z$ -axis position determination [Fig. 1(a)]. Additionally, the cellular orientation and the flagellar configuration are observed by strobe fluorescence microscopy [Fig. 1(a)]. Our approach capitalizes on the sheathed structure of *A. fischeri*'s flagella, allowing us to employ lipophilic dyes to simultaneously label the cell's membrane and flagella [24–26].

The number of flagella in *A. fischeri* is regulated by  $[\text{Mg}^{2+}]$  [20,21] and the flagellar motor is driven by  $[\text{Na}^+]$  [27]. Using phase-contrast 3D tracking, we found *A. fischeri* swims in straight lines with sudden angle changes [Fig. 1(b)] and the average swimming speed saturates at approximately 66  $\mu\text{m}/\text{s}$  in  $[\text{Mg}^{2+}] = 50$  mM and  $[\text{Na}^+] \geq 30$  mM (SM [22], Fig. S2A). When equipped with only a single flagellum, *A. fischeri* maintains an average saturated swimming speed of about 45  $\mu\text{m}/\text{s}$  when  $[\text{Mg}^{2+}]$  is entirely absent and  $[\text{Na}^+]$  remains at 30 mM. The optimal performance can be achieved at  $[\text{Mg}^{2+}]$  levels of 2 mM or greater (SM [22], Fig. S2A).

Interestingly, we found alternating speeds during swimming angle changes in *A. fischeri* [Fig. 1(b)]. Within straight swimming segments, the speed remains consistent, with faster and slower speeds exhibiting an approximate twofold difference. This phenomenon persists across different flagellar

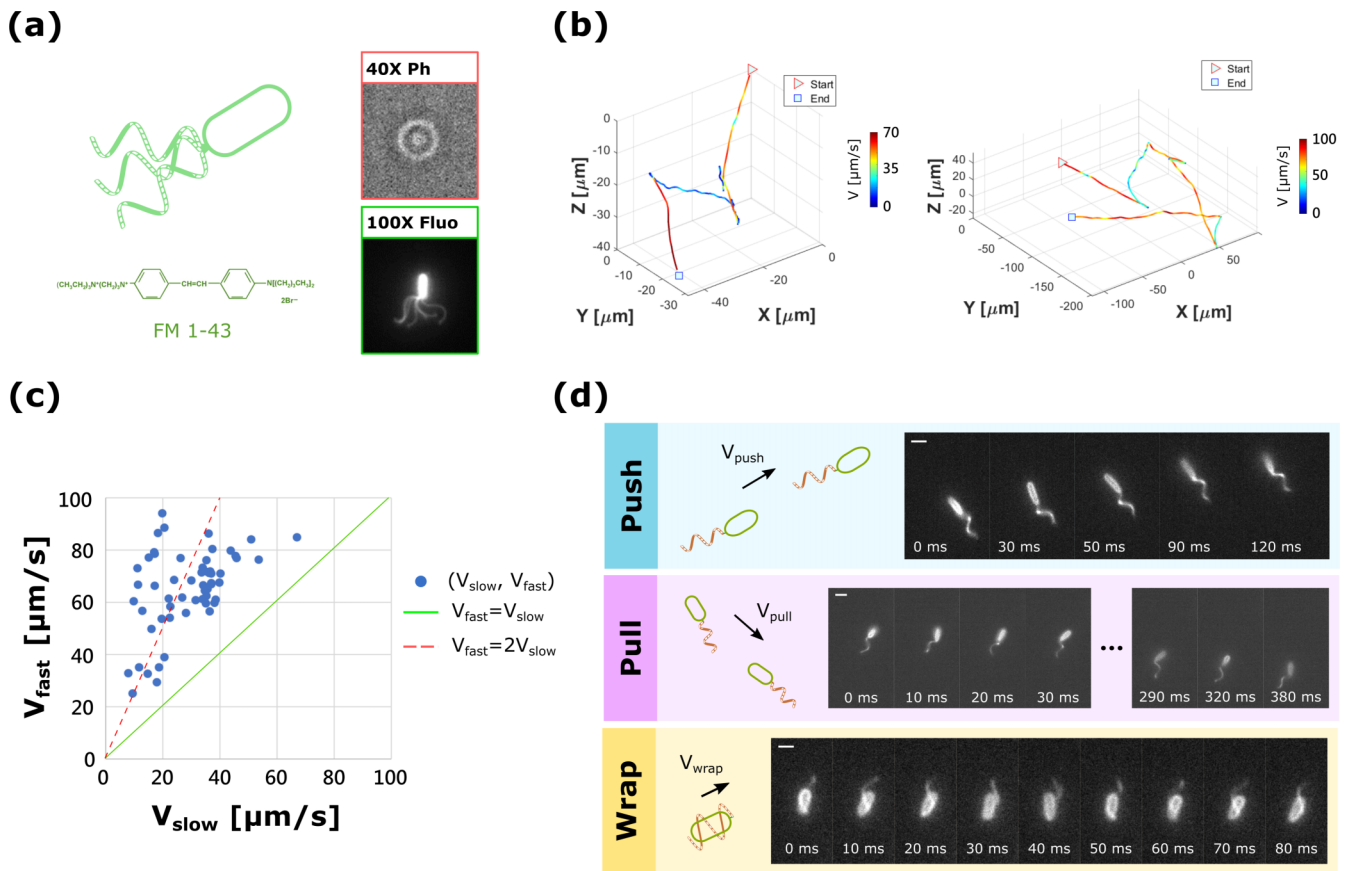


FIG. 1. *A. fischeri* 3D tracking and motile modes. (a) *A. fischeri* is a sheathed lophotrichous bacterium. Bacterial positions were determined by comparing asymmetry out-of-focus diffraction images to a reference library [18]. The cell body orientation and flagellar configuration were observed using strobe fluorescent microscopy with a lipophilic dye FM 1-43. (b) Reconstructed single-cell swimming traces of *A. fischeri* reveal two distinct alternating swimming speed segments, separated by an abrupt change in swimming angle. (c) The fast swimming speed is approximately twice as fast as the slow swimming speed across various energetic conditions ( $N = 58$  cells). (d) *A. fischeri* exhibits multiple motile modes, including push, pull, and wrap modes. A sequence of fluorescent micrographs illustrates the cell body, flagellar filament configuration, and swimming direction. The time is indicated in each image and the scale bar represents 2  $\mu\text{m}$ .

expression levels and driving ion motive forces, as depicted in Fig. 1(c), red dashed line. While Kinoshita *et al.* reported two distinct swimming speeds for *A. fischeri* in forward and wrap modes [8], it is crucial to note that swimming patterns are influenced by factors such as bacterial morphology [18], flagellar arrangements [11,12], and flagellar configurations and properties [28]. In our investigations, we have verified that the cellular morphology of *A. fischeri* remains consistent across varying flagellar expression conditions. Consequently, the crux of understanding *A. fischeri*'s swimming behavior revolves around decoding its flagellar configurations.

This bacterial species exhibits flagellar rotations at speeds exceeding 200 Hz, as determined through back-focal-plane interferometry [29]. There are several attempts to visualize flagellar configuration during natural swimming conditions using darkfield microscopy [30] and fluorescence microscopy [6,7,31] and TIRF [8]. However, capturing clear, real-time flagellar configurations and polymorphisms under natural swimming conditions remains a challenging endeavor due to the slender cross-section and rapid rotational motion of flagellar filaments.

Our approach leverages the sheathed nature of *A. fischeri*'s flagella, which we label with the lipophilic dye

FM 1-43. To facilitate a comprehensive observation of flagellar configurations at large field of view, we have implemented strobe-illumination fluorescence microscopy during *A. fischeri*'s swimming activities. This method involves maintaining camera frame rates at 33.3/100 frames per second (fps), with the fluorescence excitation illumination duty ratio consistently set at 0.5%/2% (SM [22], Fig. S3, Movie S1). We found the flagellar motion of *A. fischeri* can be categorized into three primary modes: push, pull, and wrap [Fig. 1(d)].

### B. Viscosity-dependent motility and wrap-mode trapping

In this study, we define the forward motion as the cell's movement toward the end without flagellum. In a standard water environment with a viscosity of 0.89 cP, the prevailing swimming pattern of *A. fischeri* is push-pull motions. However, when the viscosity increases to 1.53 cP, the duration of the wrap mode extends to encompass approximately 50% of the backward motion [Fig. 2(a), middle]. Further elevations in viscosity to 1.94 cP result in the wrap mode taking precedence over backward motion, with forward-type swimming becoming a rare occurrence [Fig. 2(a), bottom]. In contrast to *Shewanella putrefaciens* [7], the swimming modes of

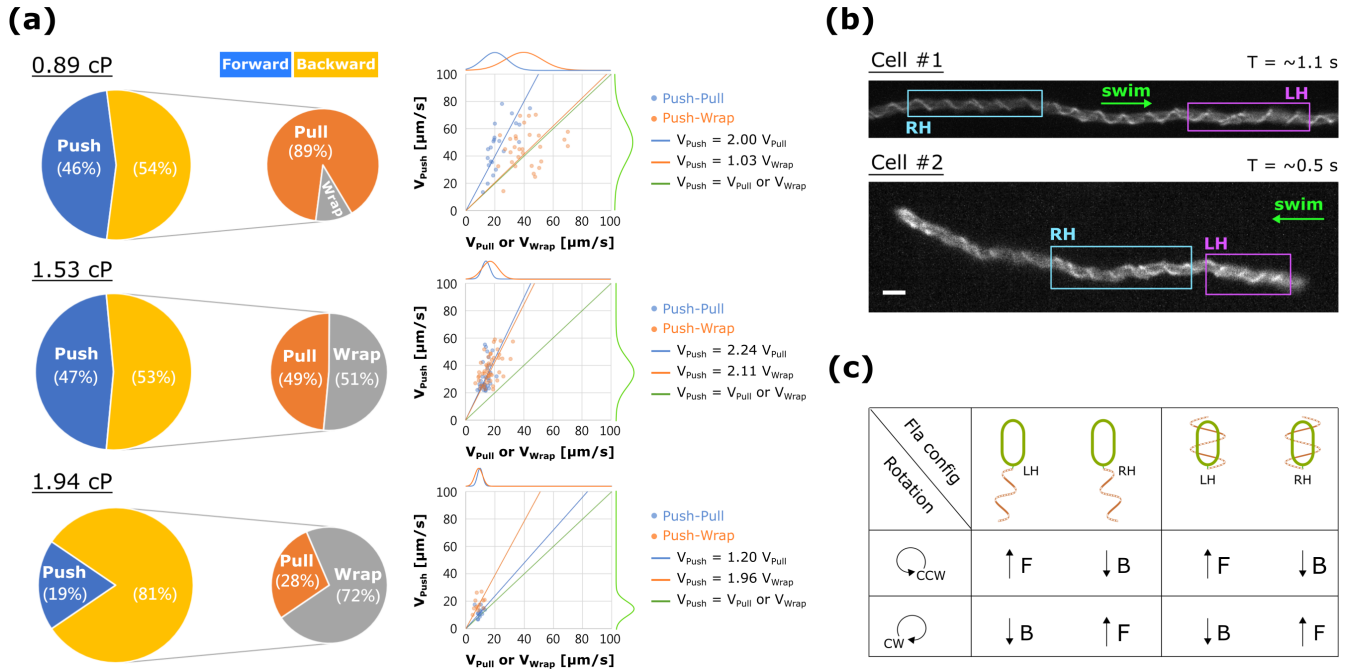


FIG. 2. Viscosity-dependent motility patterns of *A. fischeri*. (a) Viscosity-dependent motility patterns and speeds. The probability of different swimming modes ( $N = 331, 897, \text{ and } 532$  events for viscosities of  $0.89 \text{ cP}$ ,  $1.53 \text{ cP}$ , and  $1.94 \text{ cP}$ ) is depicted alongside a scatter plot of speeds ( $N = 52, 79, \text{ and } 25$  cells for  $0.89 \text{ cP}$ ,  $1.53 \text{ cP}$ , and  $1.94 \text{ cP}$ ) in varying viscous environments. Under standard water viscosity ( $0.89 \text{ cP}$ ), the forward/backward swimming ratio is approximately equal and the primary motile pattern observed is push-pull modes. As viscosity increases slightly ( $1.53 \text{ cP}$ ), the pull mode decreases and the wrap mode becomes more prominent. At even higher viscosity ( $1.94 \text{ cP}$ ), the motile pattern is dominated by push-wrap, with a prevalence of backward swimming. (b) Flagellar polymorphic transitions at higher viscosity. Under higher viscosity conditions, flagellar polymorphic transitions are observed while cells maintain their swimming direction. Strobe fluorescence images in maximal intensity projection reveal that a significant fraction of backward motion arises from left-handed (LH) and right-handed (RH) flagellar filaments during the wrap mode. The scale bar is  $2 \mu\text{m}$ . (c) Summary of swimming direction (forward/backward) relative to motor rotation direction (CCW/CW), flagellar handedness (LH/RH), and configuration (tailed/wrapped).

*A. fischeri* exhibit remarkable sensitivity to environmental viscosity. As viscosity increases, swimming speed decreases as anticipated. Interestingly, the wrap mode becomes predominant with only a twofold increase in viscosity.

To investigate swimming behavior under high-viscosity conditions, we employed strobe fluorescence microscopy to observe flagellar configurations. Surprisingly, we observed the presence of both left-handed (LH) and right-handed (RH) flagella during the wrap mode [Fig. 2(b)] when the cell moves backward. This suggests the existence of motor rotational direction switching concurrent with the flagellar polymorphic transition, which helps maintain a consistent swimming direction [Figs. 2(b) and 2(c) and Movie S2 [22]]. This phenomenon is rooted in the fact that the swim direction (forward/backward) is influenced by the flagellar motor’s rotational direction [clockwise (CW)/counterclockwise (CCW)], flagellar handedness (RH or LH), and the flagellar configuration (either tailed or wrapped) [Fig. 2(c)]. To maintain the same swimming direction, flagellar handedness transformation must accompany the motor rotational direction switching. For *A. fischeri*, wrapping is more common in high-viscosity environments. The coupling of the flagellar polymorphic transition and flagellar motor switching ensures the persistence of the backward wrap mode. Consequently, *A. fischeri* reduces the probability of switching back to forward motion and becomes entrapped in the wrap mode. Notably, the flagellar polymorphic transition occurs rapidly,

within less than  $10 \text{ ms}$ , ensuring the integrity of the flagellar bundles.

### C. Mode transitions and complete swimming patterns

To obtain a comprehensive understanding of swimming patterns, it is essential to examine the transitions between motile modes. In our strobe fluorescence microscopy observations, we identified motile mode transitions following the sequence of push-pull-wrap-push (Fig. 3). *A. fischeri* is a lophotrichous bacterium, meaning that, in the push mode, the cell body moves forward and all motors rotate in the CCW direction. Conversely, in the pull mode, when the motors switch to the CW direction, the cell body moves backward as shown in Fig. 3(a).

During the pull mode, the filaments may bend at an angle relative to the cell axis, as seen in Fig. 3(a), cell no. 2, at times between  $0.20$  and  $0.37 \text{ s}$ . If the bending angle is significant, the filament wraps around the cell body. Upon further analysis of wrap transitions, we identified two types of wrapping processes. The first type occurs when all bacterial flagella bundle into a curved shape due to instability at the hook—the junction between the body and the filament. This causes the flagella to fold directly around the bacteria and wrap around the cell body [Fig. 3(a), cell no. 2]. Therefore, we measured the critical angle, denoted as  $\theta_c$ , between the cell axis and the maximum flagellar filament deviation axis as

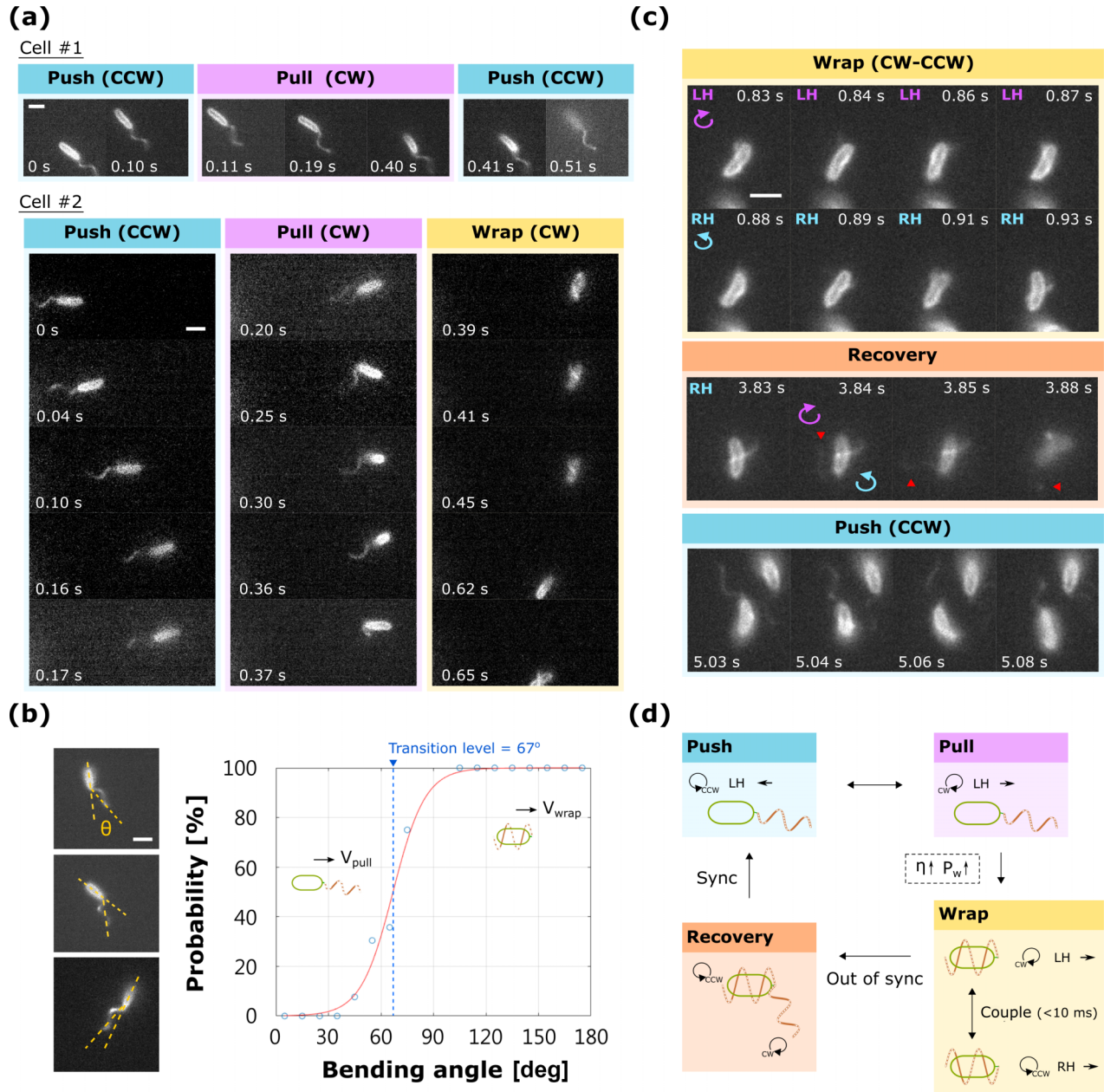


FIG. 3. Motile mode transitions in *A. fischeri*. Scale bar: 2  $\mu\text{m}$ . (a) Example traces of individual cells. Cell 1 exhibits a transition from push (CCW) to pull (CW) and then returns to push (CCW) mode. Cell 2 demonstrates transitions from push (CCW) to pull (CW) and then to wrap (CW) modes, along with a flagellar polymorphic transition from push to wrap mode. (b) Transition curve illustrating the shift in flagellar configuration from pull mode to wrap mode. Data points are marked by blue circles and the red line represents the fitted curve. (c) Example trace of a cell undergoing a transition from wrap mode. During wrap mode, the cell undergoes a coupled motor switching (CW to CCW) and a flagellar polymorphic transition (LH to RH). Subsequently, the cell transitions back to CW and LH states, followed by another motor switch and a recovery transition from wrap mode to push mode. Purple circular arrows, blue circular arrows, and red triangles represent CW rotation, CCW rotation, and escaped filaments, respectively. (d) Complete swimming patterns of *A. fischeri*. Three primary motile modes are observed: push, pull, and wrap modes. Under low viscosity conditions, *A. fischeri* predominantly engages in push-pull motion, with rare transitions to the wrap mode. In high-viscosity environments, CCW-CW switching induces a transition from push to pull mode, quickly followed by filament wrapping and polymorphic transitions. In wrap mode, CW-CCW switching may couple to flagellar polymorphic transitions to maintain the wrap mode or initiate a recovery step back to the push mode.

depicted in Fig. 3(b). To determine the transition angle, we applied a common activation sigmoid function:

$$P(\theta) = \frac{1}{1 + e^{-\alpha(\theta - \theta_c)}}. \tag{1}$$

Here,  $\alpha = 0.1082$  represents the steepness and  $\theta_c = 66.9 \text{ \AA}$  is the critical angle. It is important to note that increasing viscosity leads to a higher occurrence of the wrap mode [Fig. 2(a)], resulting in a very brief lifetime for the pull mode [7].

The second type of wrapping, which is rarer and generally observed in the transition from pull to wrap motion, involves the flagella unbundling and spreading around the cell body (SM [22], Fig. S4). Once the flagella synchronize, the filament wraps around the cell body. Both types of wrapping require motor switching and flagellar polymorphic transformation. We also observed that, at higher viscosity conditions, the pull mode is almost negligible and cells rapidly shift from the push mode to the wrap mode [7].

From these qualitative results, we can infer that the flagellar filaments exert a significant torque when the flagellar motor switches from CCW mode to CW mode. Similar to the *V. alginolyticus* hook buckling effect to induce flagellar flick motion, *A. fischeri*'s filament bends and this torque-generating force brings the normal-type flagellar filament into a polymorphic transformation. As a result, the flagellar filament becomes a semicoiled state similar to *E. coli* [31] and eventually wraps around the cell body.

The process by which *A. fischeri* transitions from the wrap mode to the push mode is a crucial step in understanding the complete swimming pattern. Figure 3(c) provides an example trace of this process. In high-viscosity conditions, cells become trapped in the wrap mode, where motor switching induces flagellar polymorphic transitions. This process requires the synchronized action of all flagella. If one molecular motor falls out of synchronization with the others during the rotation-switching process, the flagella unwind until synchronization is restored. This process is analogous to that observed in *E. coli*, where peritrichous bacteria swim by rotating their flagella, forming a bundle when the flagellar motor rotates in the CCW direction. When one or more motors rotate in the CW direction, the flagellar bundle is unraveled. In some extreme cases, we observed that all flagella lose synchronization and unwind (SM [22], Fig. S5). This recovery process necessitates that at least one of the flagella falls out of synchronization.

With the help of high spatial-temporal resolution images, we reconstructed the complete swimming patterns of *A. fischeri* [Fig. 3(d)]. In low-viscosity environments, the bacteria exhibit back-and-forth movement in the push and pull modes. However, as the environmental viscosity increases, the applied torque during the switching process induces a transition to the wrap mode. The high coupling probability of flagellar switching and flagellar polymorphic transition causes cells to become trapped in the wrap mode. Transitioning back to the pull mode is only possible when the flagella fall out of synchronization.

While the wrap mode allows for bacterial escape [11,12] or efficient chemotactic drift [9,10], the advantages of this extended wrap mode remain unclear. Therefore, in the subsequent simulation section, we delve into whether extending the backward runtime offers any benefits to the swimming process of *A. fischeri*.

#### D. Chemotaxis of *A. fischeri* relies on extending CCW duration

To investigate the chemotaxis mechanism of *A. fischeri*, we conducted chemotaxis experiments using an agarose-plug assay [32] (see SM [22]). The chemotaxis chamber was constructed using a microscope slide and a cover glass separated

by a 240  $\mu\text{m}$  spacer. A circular agar pad of approximately 1.5 mm in diameter, composed of 3% agarose and either a designed attractant (10 mM L-serine) or medium, was placed in the center of the chamber. Diluted cells were subsequently introduced into this chemotactic chamber for observation [Fig. 4(a)]. To manipulate the viscosity of the medium, we adjusted it by varying the glycerol concentration.

Utilizing phase-contrast 3D tracking microscopy, we measured the distribution of swimming speeds under three different chemotactic conditions: no attractant, constant attractant, and attractant gradient. We applied a population-based approach to obtain runtime measurements. Initially, we collected speed traces from individual cells [Fig. 4(b), left] and then employed a bimodal equation to fit the speed distribution containing state speeds ( $V$ ) and probabilities ( $P$ ) [Fig. 4(b), right].

In low-viscosity environments where the wrap mode rarely occurred [Fig. 2(a)], the two speeds corresponded to the forward push (CCW) and backward pull (CW) modes. Consequently, we obtained values for forward speed ( $V_f$ ), backward speed ( $V_b$ ), forward probability ( $P_f$ ), and backward probability ( $P_b$ ) through bimodal fitting [Fig. 4(b)]. The ratio of the average forward runtime ( $\langle T_f \rangle$ ) to the backward runtime ( $\langle T_b \rangle$ ), represented as  $\beta$ , is equivalent to the ratio of state probabilities:

$$\beta = \frac{\langle T_f \rangle}{\langle T_b \rangle} = \frac{P_f}{P_b}. \quad (2)$$

We observed  $\beta$  values of 0.52, 0.54, and 1.56 for the no attractant, constant attraction, and attraction gradient conditions, respectively. In the presence of an attractant gradient, *A. fischeri* exhibited a preference for the push mode, resembling *E. coli*, where bacteria extend their CCW motor rotation duration when moving toward a chemical gradient [5].

Next, we determined the drift angle of *A. fischeri* under these three conditions [Fig. 4(c), top]. The radar map illustrated that *A. fischeri* did not exhibit a directional bias in homogeneous environments, whether in the absence of an attractant or under uniform attractant conditions. However, a clear chemotaxis response was observed when cells navigated upward toward the attractant source.

Given the variations in swimming speeds exhibited by states of *A. fischeri*, we introduced a swim length ratio ( $\gamma$ ) to quantify the differences in chemotaxis behavior between gradient and homogeneous environments:

$$\gamma = \frac{L_f}{L_b} = \frac{V_f \langle T_f \rangle}{V_b \langle T_b \rangle} = \frac{V_f P_f}{V_b P_b}. \quad (3)$$

In the absence of a chemical gradient in the environment, although  $V_f$  was about twice that of  $V_b$ , the relationship  $2\langle T_f \rangle = \langle T_b \rangle$  led to a final  $\gamma$  value of approximately 1. This indicated that the overall swimming length in the forward mode was equivalent to that in the backward mode. In the presence of an attractant gradient, we observed  $\gamma = 3.54$ , signifying that the forward swimming length was much more than the backward swimming length [Fig. 4(c), bottom]. In essence, *A. fischeri* displayed a forward swimming bias in a chemotactic gradient environment.

In higher viscosity conditions, the wrap mode became predominant. The rotary switching and coupled polymorphic transition significantly extended the duration of backward

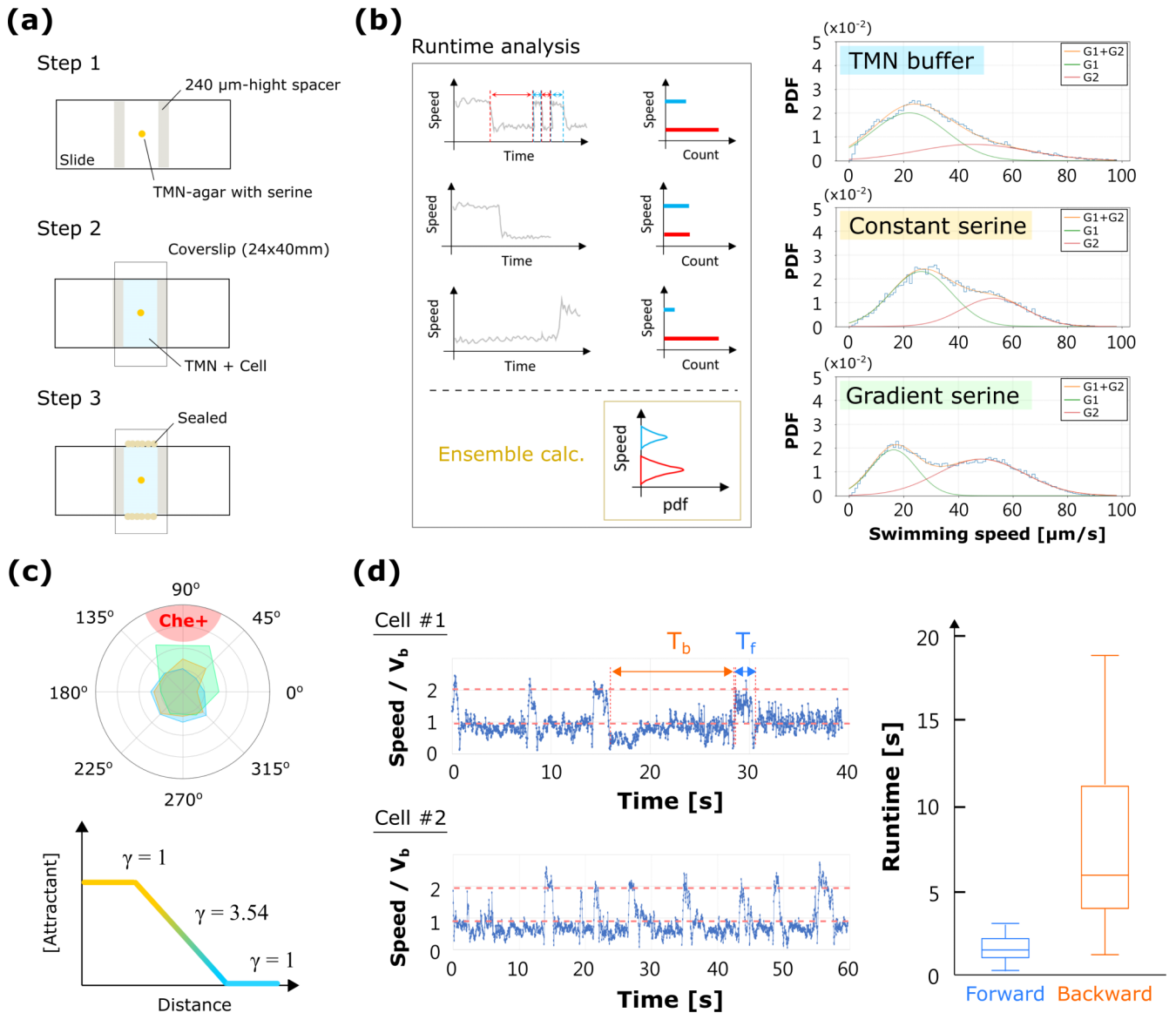


FIG. 4. Chemotaxis experiment. (a) Schematic representation of the chemotaxis chamber. (b) Left: analysis methods. Single-cell speed traces were collected and used for population speed histogram. Right: speed histogram of cells in homogeneous and gradient environments. The number of cells analyzed is provided:  $N = 150$  for no attractant (TMN buffer),  $N = 106$  for constant attractant (L-serine), and  $N = 258$  for attractant gradient (L-serine). (c) Radar map displaying the drifting direction of cells in three different environments: TMN buffer (blue), constant attractant (yellow), and attractant gradient (green). Cells in attractant gradient environments exhibit a pronounced chemotactic attraction toward the attractant source. (d) Runtime measurements at high viscosity. Two sample speed traces of cells demonstrating variations in fast forward and slow backward swimming speeds (left). The forward runtime  $T_f$  and backward runtime  $T_b$  can be obtained. Forward runtime ( $N = 32$ ) is shorter than backward runtime ( $N = 34$ ) (right).

motion, by up to 2.54 times. Since the backward swimming in the wrap mode at higher viscosity encompassed both CCW and CW motor rotation times, we were able to estimate the CCW and CW runtime duration through the following equations. In chemotaxis experiment without any attractant, we obtained the  $\beta_{0.89cP} = 0.52$  and  $\beta_{1.94cP} = 0.20$  [Fig. 4(d)]. If we assume that the motor switching rate is independent of the viscosity, we can write down the following equations:

$$\beta_{0.89cP} = \frac{\langle T_f \rangle}{\langle T_b \rangle} \Big|_{0.89cP} = \frac{\langle T_{CCW} \rangle}{\langle T_{CW} \rangle} = 0.52, \quad (4)$$

$$\beta_{1.94cP} = \frac{\langle T_f \rangle}{\langle T_b \rangle} \Big|_{1.94cP} = \frac{\langle T_{CCW} \rangle}{n(\langle T_{CCW} \rangle + \langle T_{CW} \rangle)} = 0.20. \quad (5)$$

From these equations, we determined the number of coupling pairs to be  $n = 1.71$ . This implied that we could observe this interesting event approximately twice in a wrap mode at 1.94 cP. Furthermore, the mean runtime of CCW and CW was approximately 1.75 s and 3.5 s, respectively [Fig. 4(d), right].

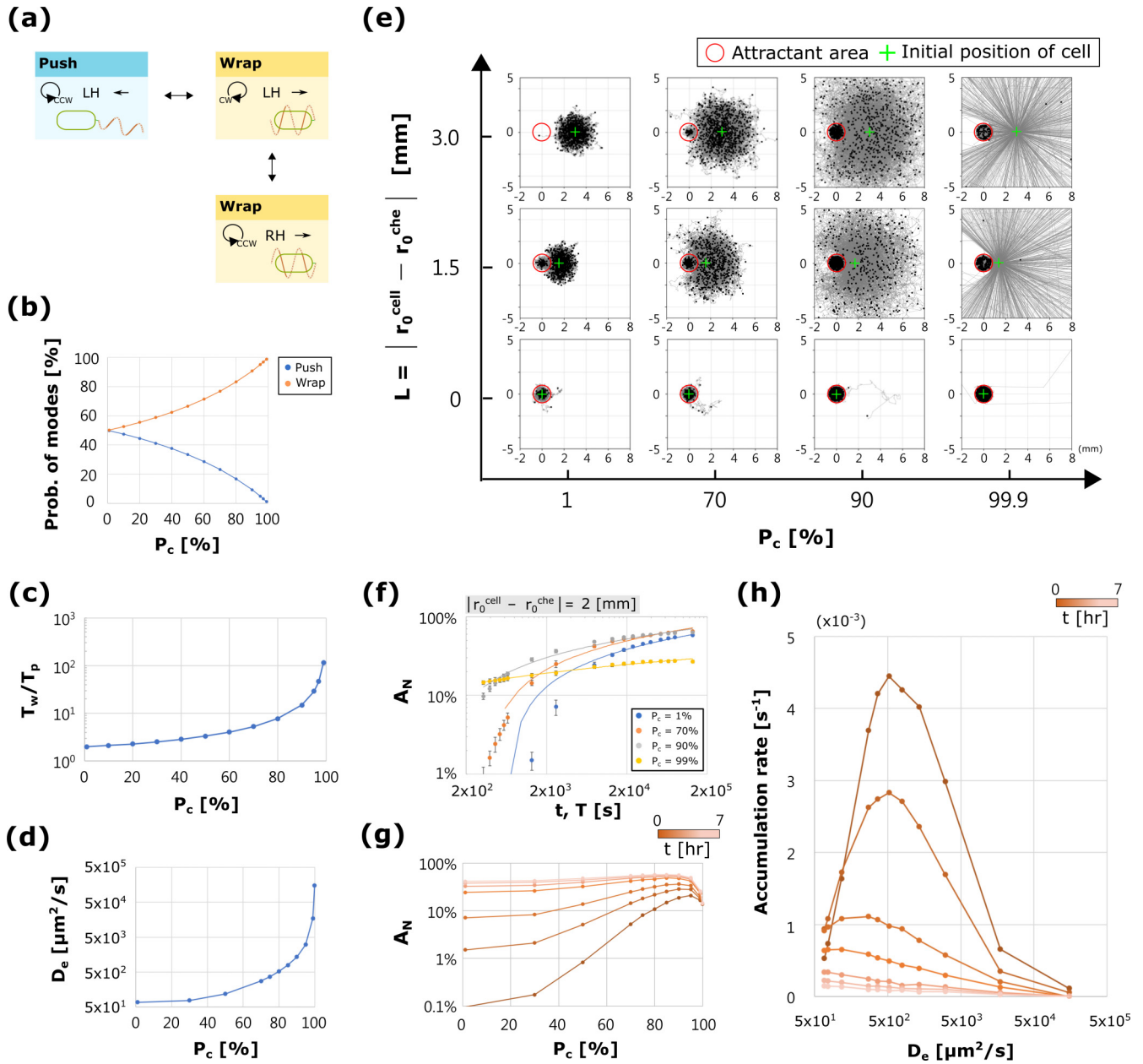


FIG. 5. Numerical simulation. (a) Simplified swimming pattern in high-viscosity environments. (b) Probability of swimming modes for different coupling probabilities ( $P_c$ ). (c) Ratio of mode durations as a function of  $P_c$ . (d) Increase in the effective diffusion constant  $D_e$  with increasing  $P_c$ . (e) Simulated swimming paths at various distances from the attractant for different values of  $P_c$ . Attractants are positioned at the origin and each simulation spans 1000 time steps. (f) Accumulation probability ( $A_N$ ) over time for different  $P_c$  values. (g) Accumulation probability as a function of  $P_c$ . (h) Time evolution of the accumulation rate for different effective diffusion constants. The results were consistent across 50 repeated numerical simulations.

### E. Active particle model with viscosity-dependent swimming pattern

In order to elucidate the impact of wrap mode trapping on the chemotactic performance of *A. fischeri*, we developed an active particle model based on the observed swimming patterns, as depicted in Fig. 3(d) [9]. Under conditions of higher viscosity, we modeled *A. fischeri* as exhibiting two distinct run modes: forward (push) and backward (wrap) swimming, as shown in Fig. 5(a). Throughout these run modes, cells moved

at characteristic speeds, denoted as  $V_p$  and  $V_w$ , representing push and wrap motion, respectively. Mode transitions were solely initiated by motor switching and the switching time was considered negligible. These mode durations were assumed to follow exponential distributions, allowing us to characterize them by their average duration or an effective transition rate.

Unlike other bacteria that exhibit a simple wrap mode, *A. fischeri* demonstrated coupled motor switching and polymorphic transformation. In light of this behavior, we introduced

TABLE I. Parameters for the computational model.

Parameters	Symbol	Value	Ref.
Push mode speed	$V_p$	16 $\mu\text{m/s}$	In this study
Wrap mode speed	$V_w$	8 $\mu\text{m/s}$	In this study
Mean CCW runtime	$\tau_0^{\text{CCW}}$	1.75 s	In this study
Mean CW runtime	$\tau_0^{\text{CW}}$	3.50 s	In this study
Mean turn angle	$\psi$	150°	Alirezaeizanjani <i>et al.</i> [9]
Normal coupling probability	$P_c^N$	70%	In this study
Attractant coupling probability	$P_c^A$	1%	In this study
Motor gain	$K$	3 $\mu\text{M}^{-1}$	In this study
Minimal response concentration	$C_{\text{response}}^{\text{min}}$	0.1 $\mu\text{M}$	Sagawa <i>et al.</i> [41]
Receptor saturation concentration	$C_{\text{receptor}}^{\text{max}}$	100 $\mu\text{M}$	Sourjik <i>et al.</i> [42]
Attractant source concentration	$C_0$	10 mM	In this study
Attractant distribution STD	$\sigma$	200 $\mu\text{m}$	Gundlach <i>et al.</i> [36]

a coupling probability, denoted as  $P_c$ , to describe the transition probability from wrap mode (CW, LH) to wrap mode (CCW, RH), as illustrated in Fig. 5(a). During this transition, all motors switched, and flagellar filaments changed their handedness. Unsuccessful transition events involved cells transiting from wrap mode (CW, LH) to push mode (CCW, LH) through a negligible short-term recovery process. Transitioning from wrap mode (CW, LH) to wrap mode (CCW, RH) involved no changes in swimming direction, with cells maintaining a straight-line trajectory. Transitions between push and wrap modes, or vice versa, induced reversals in the swim direction due to flagellar configuration changes. The turn angle distribution  $\psi$  exhibited a peak around  $\psi \approx 180^\circ$ , with an average  $\psi \approx 150^\circ$  (see SM [22]) [9]. The rotation Brownian motion is excluded in the simulation to demonstrate the sole effect of the coupling probability. Further details of the model and simulation are provided in the Supplemental Material [22]. The parameter set utilized to generate the results presented in the main text is provided in Table I.

For simplicity, we assumed that the pull mode was eliminated under conditions of high viscosity (greater than 1.94 cP) and we assigned probabilities of 25% for push mode and 75% for wrap mode, respectively. Additionally, we considered the duration of wrap mode to be five times longer than that of push mode, resulting in a value of  $\beta_{1.94\text{cP}} = 0.20$ . We conducted simulations using different  $P_c$  values and observed that both wrap mode probability [Fig. 5(b)] and the wrap-to-push mode runtime ratio ( $1/\beta$ ) [Fig. 5(c)] increased with  $P_c$ . Our simulations revealed that normal coupling probability  $P_c^N = 70\%$  provided a good match with a wrap mode probability of approximately 75% [Fig. 5(b)] and  $1/\beta_{1.94\text{cP}} = 5.0$  [Fig. 5(c)]. However, when *A. fischeri* was exposed to an attractant gradient, the wrap mode probability decreased to about 50%, prompting us to set attractant coupling probability  $P_c^A$  to 1% under these attractant conditions. The reduction of coupling probability may be due to the motor switching direction asynchronously.

Bacterial swimming patterns can be effectively characterized in terms of bacterial diffusion, with the description being governed by an effective diffusion constant  $D_e$  [4,33]. To describe the swimming of a cell in 2D at a constant speed  $V$ , subject to exponentially distributed runtime  $\tau_{\text{run}}$  and a single turn angle  $\psi$ , the effective diffusion constant is given by the

equation

$$D_e = \frac{V^2 \tau_{\text{run}}}{2 \times (1 - \alpha)}. \quad (6)$$

Here,  $\alpha \equiv \cos \psi$  represents the mean value of the cosine of the turn angles. For run-and-tumble motion and run-and-reverse motion,  $\alpha$  takes on the values 0.33 and  $-1$ , respectively.

For the complex swimming patterns exhibited by *A. fischeri*, we determined  $D_e$  through Brownian dynamics simulations by analyzing the mean-square displacement, with  $MSD = 4D_e \times t$  for 2D. We discovered a substantial increase in  $D_e$  with increasing  $P_c$ , as demonstrated in Fig. 5(d). In high-viscosity environments, *A. fischeri* with  $P_c^N = 70\%$  maintained a high  $D_e = 275 \mu\text{m}^2/\text{s}$ , surpassing *E. coli* with  $D_e = 108 \mu\text{m}^2/\text{s}$ . Upon exposure to an attractant, *A. fischeri* exhibited a reduced  $D_e = 68 \mu\text{m}^2/\text{s}$  to optimize localization efficiency.

Employing this active particle model and Brownian dynamic simulations, we explored chemotactic efficiencies under different coupling probabilities. The simulations involved positioning an attractant source at the origin and tracking the trajectories of 1000 active particles starting at predefined locations, with a distance  $L = r_0^{\text{cell}} - r_0^{\text{che}}$  from the origin, as illustrated in Fig. 5(e). The attractant concentration profile mimicked a Gaussian distribution with a  $\sigma$  that resembled the entrance to the symbiont partner's light organ. The effective radius from the attractant center is set to be the radius of the minimal response concentration [Fig. 5(e), red circle]. For cells initially located in close proximity to the attractant, the majority remained within the attraction region. The bacterial effective diffusion constant  $D_e$  increased significantly with  $P_c$ , primarily due to the extension of wrap mode runtime, as depicted in Fig. 5(e). Conversely, cells situated 2 mm away from the attractant source engaged in random-walk behaviors within a confined area, struggling to locate the attractant with  $P_c = 1\%$ . However, under high  $P_c$  (99.9%), extended runtimes caused cells to overshoot the attractant source [Fig. 5(e)]. Interestingly, intermediate coupling probability ( $P_c = 70\text{--}90\%$ ) values appeared to be optimal for searching within this range.

To quantify the searching efficiency, we computed the accumulation probability  $A_N(t)$  for the proportion of cells that successfully located an attractant area under various

conditions with simulation data. For a given searching distance and time, with  $L = 2$  mm and  $t = 1000$  time steps, the  $A_N$  was maximized for  $P_c$  in the range of 70–90%, as presented in Fig. 5(f). Intermediate  $P_c$  values extended the runtime of *A. fischeri*, enabling more effective searches within spaces of a few millimeters over a tens of minutes time frame [Fig. 5(g)].

The accumulation process was further analyzed as the aggregation of random walkers within a defined attractant area (see SM [22]). In the long-time approximation, the accumulation probability is estimated by the formula (see SM [22])

$$A_N(T) \approx \frac{(r_{\text{response}}^{\text{min}})^2}{4D} \ln \frac{4DT}{L^2}. \quad (7)$$

In this equation,  $T$  is the accumulation time and  $r_{\text{response}}^{\text{min}}$  is the radius from the center of attractants for the bacterial minimum chemotactic response. This approximation closely matched the simulation data in the long-time limit, as indicated by the solid lines in Fig. 5(f) (SM [22], Fig. S6).

In summary, in high-viscosity conditions, *A. fischeri* exhibited a dramatic increase in the effective diffusion constant  $D_e$ , exceeding values associated with run-and-tumble or run-and-reverse patterns. The maximum accumulation rate, the instant accumulation probability from the simulation data, was achieved at a  $D_e$  of approximately  $500 \mu\text{m}^2/\text{s}$  and equivalent  $P_c$  in the range of 70–80% [Fig. 5(h)]. This indicates that *A. fischeri* with  $P_c$  set at 70% is optimized for efficient navigation within spaces of a few millimeters while avoiding overshooting.

#### IV. DISCUSSION

The overall swimming patterns are shaped by various factors, including flagellar arrangements, motor rotation, flagellar filament configurations, and polymorphism. The discovery of wrap modes enhances our comprehension of bacterial flagellar movements and underscores the significance of real-time monitoring of bacterial swimming states, encompassing cell body position, orientation, and flagellar configuration. Synchronized phase contrast and fluorescence microscopy techniques have demonstrated the potential for video frame rate observation [34]. While total internal reflection fluorescence (TIRF) microscopy can offer high-quality observation, it is restricted to surface motility [8]. The primary challenge arises from the rapid rotation (hundreds of hertz) of these slender (20 nm) bacterial filaments in their natural environments. Traditional approaches using viscosity-altering agents to slow down rotation for observation may disrupt filament conformation. In this article, we demonstrate that real-time information on bacterial swimming states can be obtained by employing strobe fluorescence illumination with a standard fluorescence microscope.

As bacteria encounter high-viscosity environments, such as mucus, their swimming speeds decrease, leading to a reduction in overall diffusion constants [Eq. (6)]. Unless the mean run duration or average turning angle changes, this results in a diminished searching range. On its journey to locate a symbiotic partner, *A. fischeri* encounters challenges stemming from increased viscosity and a small target area. Interestingly,

*A. fischeri* has developed a viscosity-dependent swimming pattern as a useful alternative strategy. In low-viscosity environments, *A. fischeri* employs a push-pull swimming pattern. However, as viscosity increases, motor switching generates significant twisting and dragging forces, inducing the flagellar polymorphic transition from push to wrap modes. Once in the wrap mode, motor switching induced flagellar filament polymorphic transformation extends the backward swimming wrap mode into a longer run. This innovative approach allows for the maintenance of a larger search area in high-viscosity regions.

In essence, *A. fischeri* has developed a wrap mode in response to high viscosity, providing a competitive advantage within bacterial aggregates situated above the entrance pore on the ciliated surface of *E. scolopes*. While there is a  $600 \mu\text{m}/\text{s}$  beat flow that concentrates bacteria-sized particles (smaller than  $4 \mu\text{m}$ ) into a crypt and excludes larger particles [35,36], the complete selection rules and mechanisms that lead *E. scolopes* to specifically uptake *A. fischeri* remain unclear. However, *A. fischeri*'s wrap mode offers a significant advantage in partner recognition.

The dynamic transformation of flagellar filament polymorphism is not an isolated occurrence and is extremely dynamic [37]. In the case of *S. putrefaciens* wrap mode, the filament forms a LH helix, causing the cell to move backward [7]. Recently, Tian *et al.* observed the wrap mode in *P. aeruginosa*, wherein the filament forms a RH helix coiling around the cell body, resulting in backward movement [10]. In this article, we have identified both LH and RH wrap modes in *A. fischeri*, which can be switched between. The purpose of *A. fischeri*'s wrap mode is to extend the runtime, different from *P. aeruginosa* where the wrap mode is used for turning [10]. While we did not observe a direct transition from wrap mode (right-handed, counterclockwise) to push mode (left-handed, counterclockwise), the wrapping process in *A. fischeri* is akin to the flagellar flicking process observed in *V. alginolyticus*. We speculate that the wrapping mechanism is linked to the mechanical properties of the hook and filament [38]. The intricate details of this easy polymorphic transformation in *A. fischeri* await further investigation.

Accurately locating a specific target is a critical necessity for all biological species. Our research introduces a straightforward mechanism for bacterial chemotaxis, forming the foundational framework for understanding the highly efficient discovery of symbiotic partners. The viscosity-dependent swimming pattern we have unveiled here represents an additional mode of motility for effective environmental adaptation. It is worth noting that the buckling instability of flagellar filaments and hooks is likely prevalent among various bacterial species. The dynamic polymorphic transformation of flagellar filaments could potentially inspire the design of new active devices operating at low Reynolds numbers [39–42].

#### ACKNOWLEDGMENTS

This work was financially supported by the National Science and Technology Council, Taiwan, under Contract No. NSTC-109-2628-M-008-01-MY4 to C.J.L. C.J.L. and X.Y.Z. acknowledge the support from the National Center for Theoretical Sciences, Taiwan.

- [1] J. P. Armitage and R. M. Berry, Assembly and dynamics of the bacterial flagellum, *Annu. Rev. Microbiol.* **74**, 181 (2020).
- [2] J. A. Nirody, Y.-R. Sun, and C.-J. Lo, The biophysicist's guide to the bacterial flagellar motor, *Adv. Phys.: X* **2**, 324 (2017).
- [3] S. Nakamura and T. Minamino, Flagella-driven motility of bacteria, *Biomolecules* **9**, 279 (2019).
- [4] H. C. Berg, *Random Walks in Biology* (Princeton University Press, Princeton, NJ, 1993).
- [5] H. C. Berg and D. A. Brown, Chemotaxis in *Escherichia Coli* analysed by three-dimensional tracking, *Nature (London)* **239**, 500 (1972).
- [6] K. Son, J. S. Guasto, and R. Stocker, Bacteria can exploit a flagellar buckling instability to change direction, *Nat. Phys.* **9**, 494 (2013).
- [7] M. J. Kühn, F. K. Schmidt, B. Eckhardt, and K. M. Thormann, Bacteria exploit a polymorphic instability of the flagellar filament to escape from traps, *Proc. Natl. Acad. Sci. USA* **114**, 6340 (2017).
- [8] Y. Kinoshita, Y. Kikuchi, N. Mikami, D. Nakane, and T. Nishizaka, Unforeseen swimming and gliding mode of an insect gut symbiont, burkholderia sp. rpe64, with wrapping of the flagella around its cell body, *ISME J.* **12**, 838 (2018).
- [9] Z. Alirezaeizanjani, R. Großmann, V. Pfeifer, M. Hintsche, and C. Beta, Chemotaxis strategies of bacteria with multiple run modes, *Sci. Adv.* **6**, eaaz6153 (2020).
- [10] M. Tian, Z. Wu, R. Zhang, and J. Yuan, A new mode of swimming in singly flagellated pseudomonas aeruginosa, *Proc. Natl. Acad. Sci. USA* **119**, e2120508119 (2022).
- [11] M. Grognot and K. M. Taute, More than propellers: how flagella shape bacterial motility behaviors, *Curr. Opin. Microbiol.* **61**, 73 (2021).
- [12] K. M. Thormann, C. Beta, and M. J. Kühn, Wrapped up: The motility of polarly flagellated bacteria, *Annu. Rev. Microbiol.* **76**, 349 (2022).
- [13] J. F. Jikeli, L. Alvarez, B. M. Friedrich, L. G. Wilson, R. Pascal, R. Colin, M. Pichlo, A. Rennhack, C. Brenker, and U. B. Kaupp, Sperm navigation along helical paths in 3D chemoattractant landscapes, *Nat. Commun.* **6**, 7985 (2015).
- [14] K. L. Visick and M. J. McFall-Ngai, An exclusive contract: specificity in the vibrio fischeri-euprymna scolopes partnership, *J. Bacteriol.* **182**, 1779 (2000).
- [15] K. L. Visick, E. V. Stabb, and E. G. Ruby, A lasting symbiosis: how vibrio fischeri finds a squid partner and persists within its natural host, *Nat. Rev. Microbiol.* **19**, 654 (2021).
- [16] M.-S. Aschtgen, C. A. Brennan, K. Nikolakakis, S. Cohen, M. McFall-Ngai, and E. G. Ruby, Insights into flagellar function and mechanism from the squid-vibrio symbiosis, *npj Biofilms Microbiomes* **5**, 32 (2019).
- [17] S. V. Nyholm and M. J. McFall-Ngai, A lasting symbiosis: how the hawaiian bobtail squid finds and keeps its bioluminescent bacterial partner, *Nat. Rev. Microbiol.* **19**, 666 (2021).
- [18] K. Taute, S. Gude, S. Tans, and T. Shimizu, High-throughput 3D tracking of bacteria on a standard phase contrast microscope, *Nat. Commun.* **6**, 8776 (2015).
- [19] D. G. Christensen and K. L. Visick, *Vibrio fischeri*: laboratory cultivation, storage, and common phenotypic assays, *Curr. Protocols Microbiol.* **57**, e103 (2020).
- [20] T. M. O'Shea, C. R. DeLoney-Marino, S. Shibata, S.-I. Aizawa, A. J. Wolfe, and K. L. Visick, Magnesium promotes flagellation of *Vibrio fischeri*, *J. Bacteriol.* **187**, 2058 (2005).
- [21] T. M. O'Shea, A. H. Klein, K. Geszvain, A. J. Wolfe, and K. L. Visick, Diguanylate cyclases control magnesium-dependent motility of *Vibrio Fischeri*, *J. Bacteriol.* **188**, 8196 (2006).
- [22] See Supplemental Material at <http://link.aps.org/supplemental/10.1103/PhysRevResearch.6.033214> for the details of 3D tracking microscopy, the strobe fluorescence microscopy, the active particle model, and the simple model for accumulation probability estimation.
- [23] X.-Y. Zhuang, C.-K. Tseng, and C.-J. Lo, Live-cell imaging of the assembly and ejection processes of the bacterial flagella by fluorescence microscopy, *Bacterial and Archaeal Motility* (Springer, Berlin, 2023), pp. 35–42.
- [24] X.-Y. Zhuang, S. Guo, Z. Li, Z. Zhao, S. Kojima, M. Homma, P. Wang, C.-J. Lo, and F. Bai, Live-cell fluorescence imaging reveals dynamic production and loss of bacterial flagella, *Mol. Microbiol.* **114**, 279 (2020).
- [25] M. Chen, Z. Zhao, J. Yang, K. Peng, M. A. Baker, F. Bai, and C.-J. Lo, Length-dependent flagellar growth of *Vibrio alginolyticus* revealed by real time fluorescent imaging, *eLife* **6**, e22140 (2017).
- [26] Y. Wu, F. L. Yeh, F. Mao, and E. R. Chapman, Biophysical characterization of styryl dye-membrane interactions, *Biophys. J.* **97**, 101 (2009).
- [27] E. G. Ruby, M. Urbanowski, J. Campbell, A. Dunn, M. Faini, R. Gunsalus, P. Lostroh, C. Lupp, J. McCann, D. Millikan, *et al.*, Complete genome sequence of *Vibrio fischeri*: a symbiotic bacterium with pathogenic congeners, *Proc. Natl. Acad. Sci. USA* **102**, 3004 (2005).
- [28] M. J. Kühn, F. K. Schmidt, N. E. Farthing, F. M. Rossmann, B. Helm, L. G. Wilson, B. Eckhardt, and K. M. Thormann, Spatial arrangement of several flagellins within bacterial flagella improves motility in different environments, *Nat. Commun.* **9**, 5369 (2018).
- [29] C.-J. Lo, Y. Sowa, T. Pilizota, and R. M. Berry, Mechanism and kinetics of a sodium-driven bacterial flagellar motor, *Proc. Natl. Acad. Sci. USA* **110**, E2544 (2013).
- [30] Y. Magariyama, S.-y. Masuda, Y. Takano, T. Ohtani, and S. Kudo, Difference between forward and backward swimming speeds of the single polar-flagellated bacterium, *Vibrio alginolyticus*, *FEMS Microbiol. Lett.* **205**, 343 (2001).
- [31] L. Turner, W. S. Ryu, and H. C. Berg, Real-time imaging of fluorescent flagellar filaments, *J. Bacteriol.* **182**, 2793 (2000).
- [32] H. S. Yu and M. Alam, An agarose-in-plug bridge method to study chemotaxis in the archaeon *Halobacterium salinarum*, *FEMS Microbiol. Lett.* **156**, 265 (1997).
- [33] J. Taktikos, H. Stark, and V. Zaboruaev, How the motility pattern of bacteria affects their dispersal and chemotaxis, *PLoS One* **8**, e81936 (2013).
- [34] B. G. Hosu, W. Hill, A. D. Samuel, and H. C. Berg, Synchronized strobed phase contrast and fluorescence microscopy: the interlaced standard reimaged, *Opt. Express* **31**, 5167 (2023).
- [35] J. C. Nawroth, H. Guo, E. Koch, E. A. Heath-Heckman, J. C. Hermanson, E. G. Ruby, J. O. Dabiri, E. Kanso, and M. McFall-Ngai, Motile cilia create fluid-mechanical microhabitats for the active recruitment of the host microbiome, *Proc. Natl. Acad. Sci. USA* **114**, 9510 (2017).
- [36] K. A. Gundlach, J. Nawroth, E. Kanso, F. Nasrin, E. G. Ruby, and M. McFall-Ngai, Ciliated epithelia are key elements in the

- recruitment of bacterial partners in the squid-vibrio symbiosis, *Front. Cell Dev. Biol.* **10**, 974213 (2022).
- [37] R. Vogel and H. Stark, Rotation-induced polymorphic transitions in bacterial flagella, *Phys. Rev. Lett.* **110**, 158104 (2013).
- [38] J. Park, Y. Kim, W. Lee, and S. Lim, Modeling of lophotrichous bacteria reveals key factors for swimming reorientation, *Sci. Rep.* **12**, 6482 (2022).
- [39] M. Hu, X. Ge, X. Chen, W. Mao, X. Qian, and W.-E. Yuan, Micro/nanorobot: A promising targeted drug delivery system, *Pharmaceutics* **12**, 665 (2020).
- [40] M. Koleoso, X. Feng, Y. Xue, Q. Li, T. Munshi, and X. Chen, Micro/nanoscale magnetic robots for biomedical applications, *Mater. Today Bio* **8**, 100085 (2020).
- [41] T. Sagawa, Y. Kikuchi, Y. Inoue, H. Takahashi, T. Muraoka, K. Kinbara, A. Ishijima, and H. Fukuoka, Single-cell *E. coli* response to an instantaneously applied chemotactic signal, *Biophys. J.* **107**, 730 (2014).
- [42] V. Sourjik and H. C. Berg, Receptor sensitivity in bacterial chemotaxis, *Proc. Natl. Acad. Sci. USA* **99**, 123 (2002).